ELSEVIER

Materials Science and Engineering A 435–436 (2006) 625–631

MATERIALS SCIENCE & ENGINEERING A

www.elsevier.com/locate/msea

Analysis of thermal phenomena in LENS^{TM} deposition

Liang Wang [a], Sergio Felicelli [b,*]

[a] *Center for Advanced Vehicular Systems, Mississippi State University, Mississippi State, MS 39762, United states*
[b] *Mechanical Engineering Department, Mississippi State University, Mississippi State, MS 39762, United States*

Received 16 May 2006; received in revised form 14 July 2006; accepted 21 July 2006

Abstract

A two-dimensional finite element model was developed to calculate the temperature distribution for 316 stainless steel during the Laser Engineered Net Shaping (LENS^{TM}) rapid fabrication process as a function of time and process parameters. Numerical simulations are performed on the upper region of a thin plate part, where experimental data indicates that a uniform temperature can be assumed at the base of this region. The temperature at the base of the modeling region and the effective laser power are determined by matching predicted with previously measured temperature profiles surrounding the molten pool. Good agreement is obtained between the calculated and the measured temperature profiles. The model is then used to investigate the relative importance of physical properties and different mechanisms of heat transfer during the process. The results obtained in this work provide important and unavailable information on many thermal aspects of the LENS process.

Keywords: Laser Engineered Net Shaping; Thermal modeling; Rapid fabrication

1. Introduction

Laser Engineered Net Shaping (LENS^{TM}) is a rapid fabrication process in which three-dimensional metal structures are built layer by layer from computer aided designs (CAD). Fig. 1 shows a schematic of the LENS process. In this process, a laser beam is focused onto a substrate to create a molten pool in which powder particles are simultaneously fed. The substrate is moved beneath the laser beam under the computer guidance to deposit a thin cross section, creating the desired geometry for each layer. Starting from the bottom of the part, one layer is produced at a time. After deposition of each layer, the powder feeding nozzle and laser beam assembly is moved in the positive *Z*-direction, thereby building a three-dimensional component layer additively.

The LENS process has the potential to dramatically reduce the time and cost required to fabricate functional metal parts. Since mechanical properties are dependent upon the microstructure of the material, which in turn is a function of the thermal history of solidification, an understanding of the thermal behavior of the fabricated part during the LENS process is of special interest [1]. Unlike other laser processing techniques, LENS uses low power lasers which produce a very small heat-affected zone (HAZ). In typical applications to steel alloys, the laser power is 300–500 W, the substrate traverse velocity is about 8 mm/s, and the volume of the molten pool is about 0.5 mm^3 [2].

Several authors [1–5] performed experiments using ultra high speed digital imaging techniques during the LENS process, providing insight of the characteristics of the temperature profile, molten pool size, thermal gradients and cooling rates around and in the molten pool of 316 stainless steel (SS316) plate samples. In these experiments, the temperature along the axis of the plate was extracted from the thermal images and the temperature gradient along the travel direction was obtained by differentiating the temperature curves in the direction of travel, which can be translated to cooling rates by dividing by the traverse velocity. Fig. 2 shows the thermal profiles on the top surface of the LENS-fabricated SS316 plate from the center of the molten pool along the travel direction of the sample as a function of laser power [5]. The laser power for each profile is shown in the legend. We will use this measured data to calibrate the model developed in this work. When referring to the fabrication process, for simplicity we will consider the laser beam as moving, when in the actual process, it is the part that is translated under a fixed laser beam position.

* Corresponding author. Tel.: +1 662 325 1201; fax: +1 662 325 7223.
E-mail addresses: liangw@cavs.msstate.edu (L. Wang), felicelli@me.msstate.edu (S. Felicelli).

0921-5093/$ – see front matter © 2006 Elsevier B.V. All rights reserved.
doi:10.1016/j.msea.2006.07.087

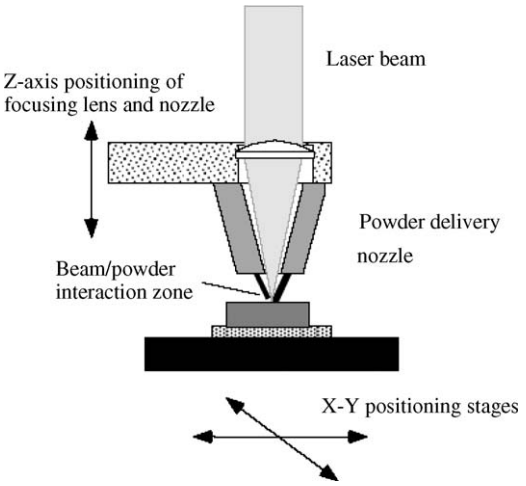

Fig. 1. Schematic of the LENS^{TM} process [4].

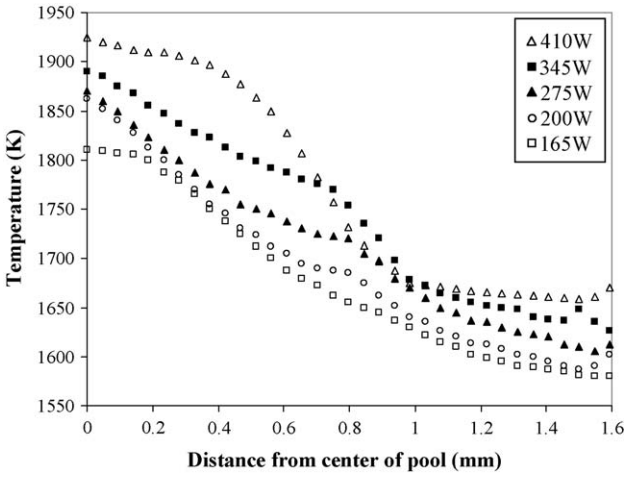

Fig. 2. Thermal profiles on the top surface of SS316 sample from the center of the molten pool along the travel direction of the sample for different laser power settings during the LENS process [5].

Numerical simulation methods have the potential to provide detailed information of the thermal behavior. Some preliminary simulation works on the thermal behavior in the LENS process have been conducted in the past [1–7]. Some of these studies estimated that more than 90% of the deposited laser energy was conducted through the substrate, and the contributions of other possible forms of heat transfer, such as heat convection and radiation from the surface of the deposited material were negligible. However, neither experimental measurements nor numerical predictions have confirmed this statement. A detailed study is necessary to investigate the importance of heat convection and radiation from the surface of the deposited material. There is also no clear information in the literature about how much the latent heat of melting affects the size of the molten pool and the temperature profiles. Grujicic et al. [8,9] developed a two-dimensional finite element model to calculate the thermal profiles in the fabricated part when the laser beam moves across the top surface of the sample. The minimum power of the laser needed to initiate melting of the part surface was predicted. However, a study of the effects of different process parameters on the thermal profiles is not available.

In this paper, a two-dimensional thermal model is developed to predict the temperature distribution in the deposited metal for SS316 during the LENS process as a function of time and process parameters. The temperature profile surrounding the molten pool in the SS316 fabricated part measured by Hofmeister et al. [5] was used to calibrate this model. In addition, test simulations for moving heat sources were verified against an existing analytical solution in the literature [10]. The significance of the different forms of heat transfer, including heat conduction, convection, and radiation from the surface of the deposited material is quantitatively investigated. The effects of variations in thermal conductivity, convective heat transfer coefficient, surface emissivity, latent heat, and laser power on the thermal profiles are investigated in a parametric study, which would be difficult to perform experimentally. The relative sensitivities of the thermal profiles and the molten pool size to the boundary conditions and laser powers are illustrated.

2. Mathematical model

In this study, numerical simulations are performed on the upper region of a thin plate fabricated by the LENS process, where experimental data indicates that a uniform temperature can be assumed at the base of this region [5]. Fig. 3 shows the schematic of the two-dimensional model used in the present work. The model uses a 25 mm × 10 mm rectangular computational domain. A laser beam of power P_l and radius w_0 moves from left to right along the top edge of the computational domain at a travel velocity v_l. The power-intensity distribution in the laser-beam cross section is assumed to be given by the following Gaussian function [9]:

$$I(x - x_0) = I_0 \exp\left(-\frac{2(x - x_0)^2}{w_0^2}\right) \quad (1)$$

where x_0 is the x coordinate of the laser-beam axis. The maximum power intensity, I_0, is defined as

$$\int_{-\infty}^{\infty} I(x - x_0)\mathrm{d}x = P_l \quad (2)$$

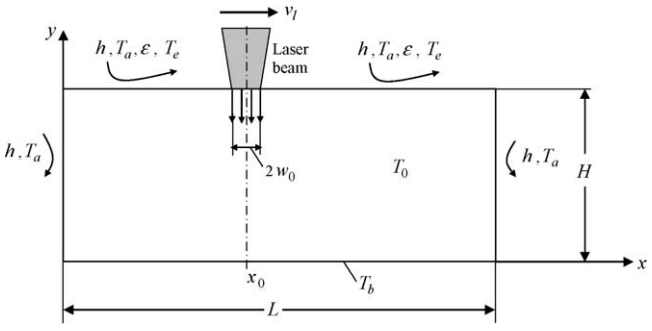

Fig. 3. Schematic of the model used for prediction of the temperature distribution in the LENS-fabricated sample.

Substituting Eq. (1) into (2) and noting that

$$\int_{-\infty}^{\infty} \exp\left(-\frac{x^2}{2}\right) \mathrm{d}x = \sqrt{2\pi} \tag{3}$$

yields:

$$I_0 = \frac{2P_\mathrm{l}}{\sqrt{2\pi} w_0} \tag{4}$$

The thermal model uses the finite element method to numerically solve the following two-dimensional energy conservation equation:

$$\frac{\partial T}{\partial t} = \kappa \left(\frac{\partial^2 T}{\partial x^2} + \frac{\partial^2 T}{\partial y^2}\right) - \frac{L}{C_p}\frac{\partial \phi}{\partial t} \tag{5}$$

where T is the temperature, t the time, κ the thermal diffusivity, L the latent heat of melting, C_p the specific heat, and ϕ is the volume fraction of liquid, approximated as

$$\phi \approx \frac{T - T_\mathrm{s}}{T_\mathrm{l} - T_\mathrm{s}} \tag{6}$$

where T_l is the liquidus temperature (1733 K), and T_s is the solidus temperature of the alloy (1693 K).

The initial condition in the computational domain is set corresponding to a uniform temperature field equal to the temperature at the base of the modeling region. The boundary conditions are defined as follows. Along the top edge of the computational domain, the following convective and radiation-based heat flux condition is used:

$$-k\frac{\partial T}{\partial y} = h(T - T_\mathrm{a}) + \varepsilon\sigma(T^4 - T_\mathrm{e}^4) \tag{7}$$

where k is the thermal conductivity, h the convective heat transfer coefficient, T_a the ambient temperature around the part, ε the emissivity of the part surface, σ the Stefan–Boltzmann constant ($\sigma = 5.67 \times 10^{-8}$ W/m^2 K^4), and T_e is the temperature of the internal wall of the glove box (taken equal to T_a in this work).

A convective boundary condition is imposed on both vertical sides of the part and given by

$$-k\frac{\partial T}{\partial x} = h(T - T_\mathrm{a}) \tag{8}$$

The bottom of the computational domain is subject to the dirichlet boundary condition:

$$T = T_0 \tag{9}$$

where T_0 a uniform temperature taken from the experiments of Hofmeister et al. [5].

The top edge of the computational domain beneath the laser beam is subjected to the following heat-flux boundary condition:

$$-k\frac{\partial T}{\partial y} = \alpha I(x - x_0) \tag{10}$$

where α is the effective absorption of the laser beam energy. After substitution of Eqs. (1) and (4) into (10) and rearrangement, the prescribed normal temperature gradient on the top surface under the beam can be written as

$$\frac{\partial T}{\partial y} = A_0 \exp\left(-\frac{2(x - x_0)^2}{w_0^2}\right) \tag{11}$$

where A_0 is given by

$$A_0 = -\frac{2\alpha P_\mathrm{l}}{\sqrt{2\pi} w_0 k} \tag{12}$$

Note that x_0 in Eq. (11) is a function of time, travel velocity of the laser beam, and the initial position of the laser beam relative to the computational domain.

Because of the limitation of two-dimensional modeling, it is not possible to establish a direct correlation between the actual three-dimensional absorbed power distribution and the idealized two-dimensional power profile used in this work. Ye et al. [6] investigated the thermal behavior in the LENS process with the finite element method. In their work, the temperatures of the nodes where the laser beam focused on were set as the melting point temperatures, thus the laser power did not actually play a role. In this study, the coefficient A_0 is determined by matching the maximum calculated temperature with the measured value reported by Hofmeister et al. [5]. By using a two-dimensional model, it is also assumed that there is no significant heat loss through the front and back surface of the part. The time evolution of the isotherms is calculated as the laser beam travels across the top surface of the part. The model dynamically updates the thermal boundary conditions with laser position; hence it is able to calculate temperature profiles both far of and near the side edges of the plate.

3. Results and discussion

The calculations of temperature distribution in a fabricated SS316 alloy plate during the LENS process are compared with measurements of thermal profiles done by Hofmeister et al. [5]. In those experiments, ultra high speed digital imaging techniques were employed to show the image of the molten pool and the temperature distribution on the surface surrounding the molten pool in SS316 samples fabricated using the LENS process. The details of the experimental setup can be found in this reference. For the purpose of comparing calculated and experimental data, similar computational parameters as that in Hofmeister's work are used, which are summarized in Table 1. The computational domain is divided into 500 × 200 bilinear finite elements, yield-

Table 1
Material properties for 316 stainless steel and LENS process parameters [5]

Parameter	Symbol	Units	Value
Density	ρ	kg/m^3	8000
Thermal conductivity	k	W/m K	21.5
Specific heat	C_p	J/kg K	500
Latent heat	L	J/kg	3×10^5
Emissivity	ε	N/A	0.62
Convective heat transfer coefficient	h	W/m^2 K	100
Radius of the laser beam	w_0	mm	0.5
Traverse velocity of the laser beam	v_l	mm/s	8.0

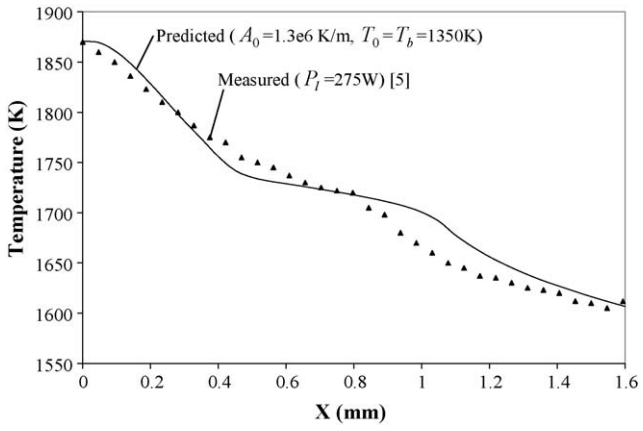

Fig. 4. Comparison of predicted and measured thermal profiles on the top surface of the sample from the center of the molten pool along the travel direction of the sample (SS316).

ing $\Delta x = \Delta y = 5.0 \times 10^{-5}$ m. This mesh was used throughout the present study. The convergence of the mesh was checked against finer discretiazations without noticeable change in the results.

Fig. 4 provides a comparison of measured and calculated thermal profiles on the top surface of the sample from the center of the molten pool along the travel direction of the sample. The calculated values are taken when the beam is at the center of the part and side effects can be neglected. The inputs used to generate the numerical results were the Gaussian function coefficient $A_0 = 1.3 \times 10^6$ K/m and a uniform temperature at the base of the domain $T_0 = 1350$ K. This temperature was measured by Hofmeister et al. [5] for an applied laser power of 275 W. The boundary conditions include a convective heat loss with $h = 100$ W/m^2 K and $T_a = 303$ K from the top and side boundaries of the part. The radiation heat loss is not considered in this calculation. The transient simulation was started from a uniform initial temperature equal to the base temperature. It is observed from Fig. 4 that the calculated temperature profile follows rather well the experimental data.

The calibrated model was then used to calculate the heat loss due to both convective heat transfer and radiation along the top surface of the sample. The results are shown in Fig. 5, for the same power settings as the previous simulation. It can be seen that the heat flux due to convection does not change much along the surface, although the magnitude surrounding the molten pool is slightly higher than that in other locations. However, the heat flux due to radiation surrounding the molten pool is significantly higher than that in both sides away from the molten pool. After integration along the top surface, the total heat loss due to convection heat transfer and radiation can be estimated at 7.5 W if the thickness of the sample is taken as 1 mm (approximately the plate thickness of Hofmeister's experiments). Therefore, for a total laser power of 275 W and an absorption coefficient of the laser beam of 0.3 [9], about 9.1% of the heat is dissipated due to convection and radiation, while the rest is conducted through the fabricated part. This result is consistent with estimates by other investigators [2], and quantitatively confirms that most of the laser energy is conducted through the part, while the heat loss by surface convection and radiation is not significant.

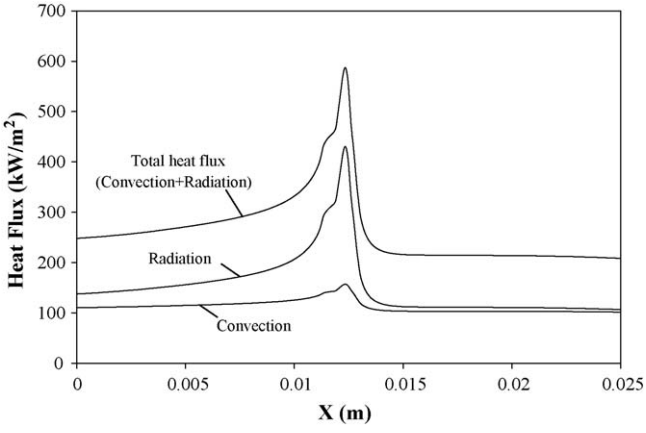

Fig. 5. Heat flux due to convection and radiation along the top surface of the sample.

Fig. 6 shows the temperature contours in the fabricated sample during the LENS process when the laser beam moves along the x positive direction at the time of 0.5, 1.5, 2.5, and 3.0 s, respectively, where time zero corresponds to the beam located at the left end of the part. Assuming no significant undercooling, the molten pool can be taken as the region with $T > 1733$ K, the liquidus temperature. The mushy zone would correspond to the region with $1693\ \text{K} < T < 1733$ K. As it can be observed in Fig. 4, for this power level, the calculated size of the molten pool is approximately 1 mm and the mushy zone is less than 0.5 mm. The pattern of heat flow shows a large temperature gradient near the melt pool, but at a distance below the top edge of about 2 mm the temperature decreases from 1850 to 1450 K and is fairly evenly distributed across the part, as shown in Fig. 6(a)–(d). It can be seen that, relative to the position of the laser beam axis, the temperature contours surrounding the molten pool are practically identical in Fig. 6(b) and (c). This finding suggests that the effects of the side edges of the computational domain are not very strong in these cases and that the temperature field has reached a steady-state condition relative to a coordinate system attached to the moving laser beam when the laser beam moves about 5 mm away from the left edge.

Using the current modeling conditions, the effects of different parameters on the thermal profiles at the top surface of the part were investigated. To eliminate the effects of the side edges, the numerical results are compared when the laser beam is at the center of the top surface at $t = 1.5$ s. The thermal profiles for different Gaussian function coefficients, corresponding to different laser powers are presented in Fig. 7. The Gaussian function coefficient for each profile is shown in the legend. Higher Gaussian function coefficients represent higher laser powers. It can be observed that the molten pool size and the pool temperature increase with the laser power.

Note that the slope of the temperature profile at the liquidus isotherm decreases significantly with the laser power. It is known that the temperature gradient can be easily converted to cooling rate by multiplying by the travel velocity. It can be concluded that increasing the laser power will reduce the cooling rate at the liquid/solid interface, which is determinant to the microstructure and the magnitude of residual stress. This agrees with the

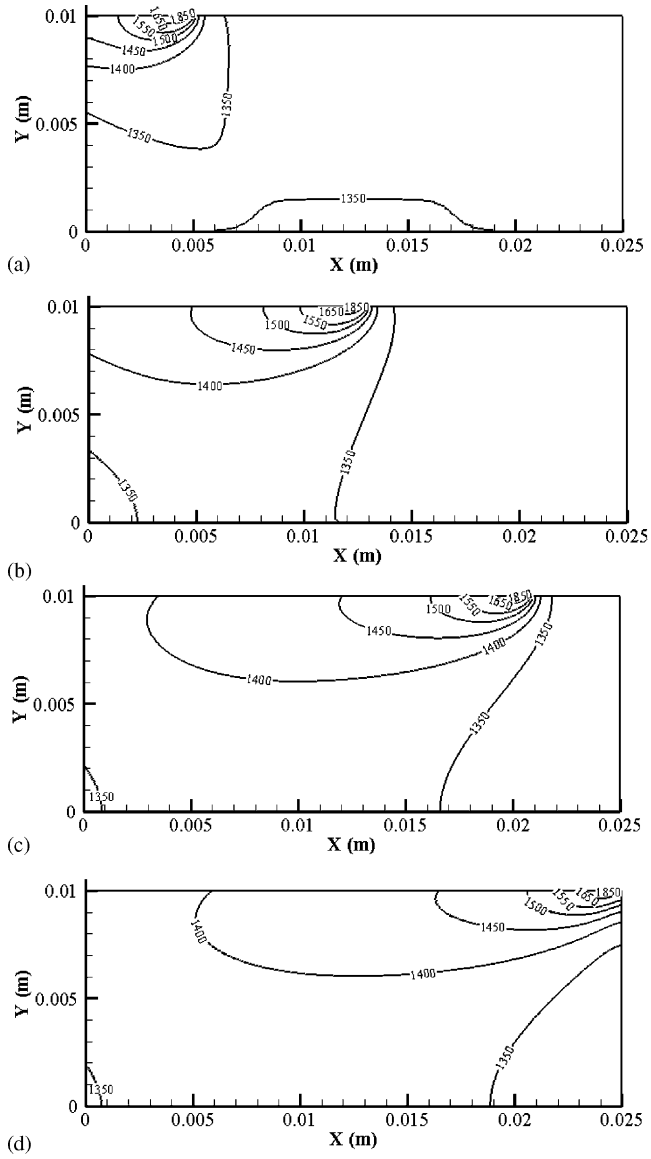

Fig. 6. Temperature contour plots at different times when the laser beam moves along the x positive direction: (a) $t = 0.5$ s, (b) $t = 1.5$ s, (c) $t = 2.5$ s and (d) $t = 3.0$ s.

experimental observations by Hofmeister et al. [5]. However, as shown in Fig. 2, the measured temperature profiles show that the molten pool size has no significant change when the laser power is greater than 275 W, while the numerical simulations continue to show a slight increase in pool size with laser power. We believe that this discrepancy is due to the effect of the inert gas flow on the convective heat transfer from the surface of the pool. Other researchers have reported experiments that show a different trend [11]. More experimental studies on the effects of the laser power on the molten pool size and cooling rates are necessary.

In the calculations, the bottom temperature is assumed to be uniform and extracted from the experimental data. The effects of different bottom temperatures on the thermal profiles are shown in Fig. 8. The length of the molten pool greatly increases with increasing bottom temperatures. Higher base temperatures can be associated to a larger preheat of the sample. However, the pool

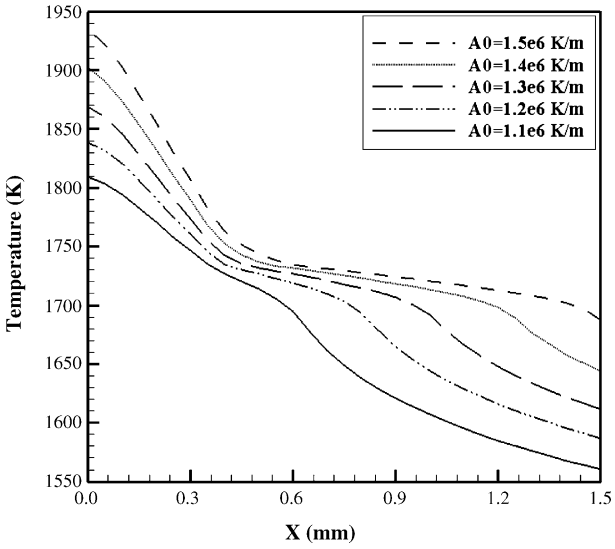

Fig. 7. Thermal profiles on the top surface of the sample from the center of the molten pool along the travel direction of the sample for different A_0 at $t = 1.5$ s.

temperature does not change significantly for different bottom temperatures. As expected, the slopes of the temperature profiles at the liquidus isotherm decrease significantly with the bottom temperature.

During the LENS process, the powder is delivered through the nozzles and driven by inert gas flow. Therefore, it is reasonable to assume that forced convection will affect the heat transfer around the laser beam position. For example, the gas-flow velocity at the powder nozzle is typically 30 m/s, correspondingly, the convective heat transfer coefficient is of the order of 10 W/m^2 K [2]. The effect of the convective heat transfer coefficient on the thermal profiles is shown in Fig. 9. It is observed that the effect of heat convection on the thermal profiles is small when the heat transfer coefficient is less than 10 W/m^2 K. For higher coefficients, the molten pool size decreases with increasing heat transfer coef-

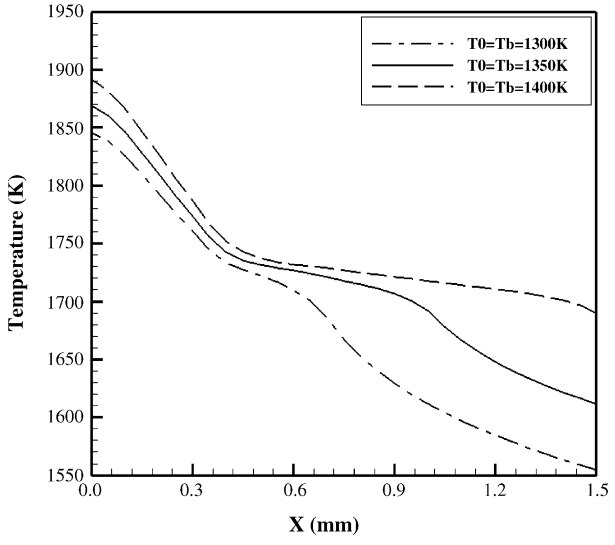

Fig. 8. Thermal profiles on the top surface of the sample from the center of the molten pool along the travel direction of the sample for different bottom temperatures and initial temperatures at $t = 1.5$ s.

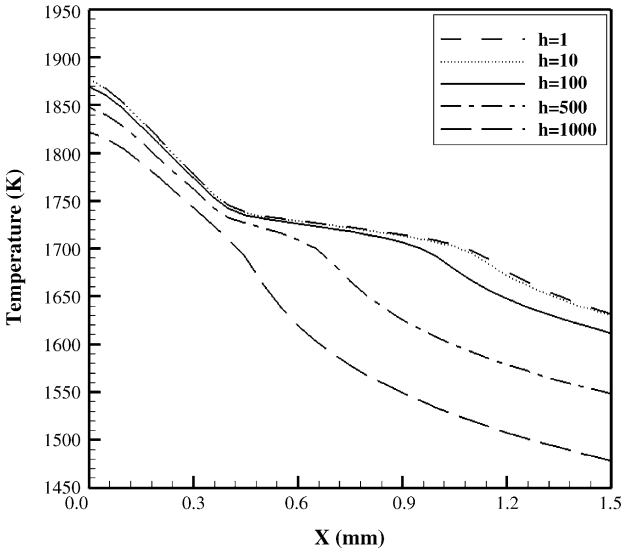

Fig. 9. Thermal profiles on the top surface of the sample from the center of the molten pool along the travel direction of the sample as a function of convective heat transfer coefficient at $t = 1.5$ s.

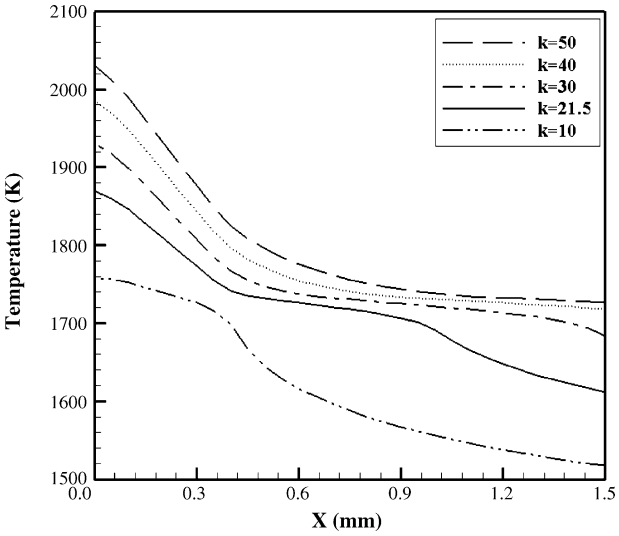

Fig. 11. Thermal profiles on the top surface of the sample from the center of the molten pool along the travel direction of the sample as a function of thermal conductivity at $t = 1.5$ s.

ficient. Note also that the pool size changes significantly for high heat transfer coefficients, but remains basically constant for low h's. This is equivalent to say that when the deposited power dominates over heat loss, the pool size stays unaffected by power changes; the excess power is conducted away through the part. This is consistent with the experimental data in Fig. 2 for high laser powers.

Fig. 10 shows the effect of latent heat of melting on the thermal profile at the top surface of the sample. The inclusion of the latent heat in the simulation produces a lower maximum temperature at the center of the liquid pool but does not change the size of the pool. In addition, the effect of the latent heat is to decrease the temperature gradient (and the cooling rate) at the liquidus isotherm.

Although in the previous calculations we used a constant thermal conductivity, it is known that the thermal conductivity of SS316 varies considerably within the range of temperatures of the process. To investigate the effect of the variation of thermal conductivity with temperature, we performed simulations with different constant values of the thermal conductivity. The results in Fig. 11 show that the length of the molten pool increases significantly with increasing heat conductivity. As expected, a higher pool temperature is obtained for higher thermal conductivity because more energy is absorbed at the same travel velocity of the laser. This suggests that it is important to include in the model the variation of thermal conductivity with temperature to correctly predict the pool size.

Fig. 12 shows the effect of radiation emissivity on the thermal profiles. It is observed that there is no significant effect in

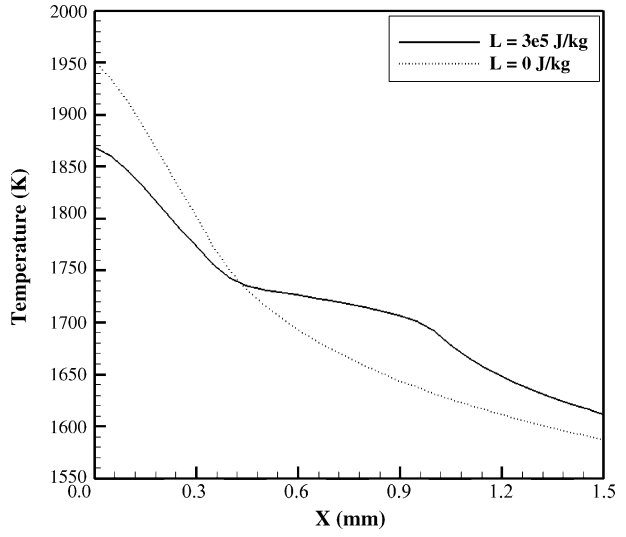

Fig. 10. Thermal profiles on the top surface of the sample from the center of the molten pool along the travel direction of the sample with and without latent heat at $t = 1.5$ s.

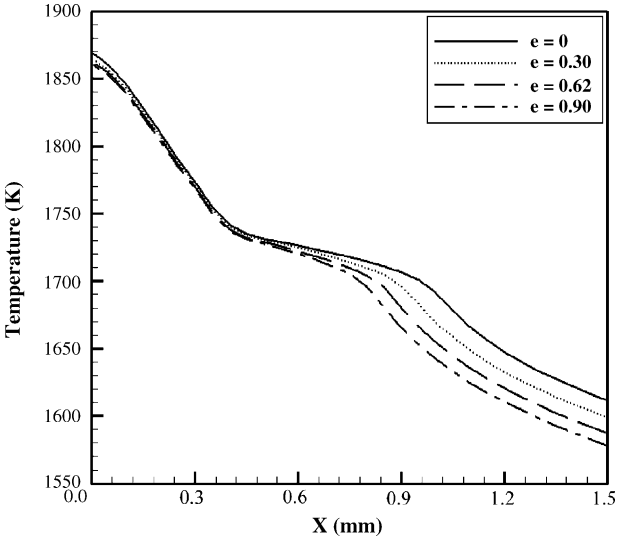

Fig. 12. Thermal profiles on the top surface of the sample from the center of the molten pool along the travel direction of the sample as a function of emissivity at $t = 1.5$ s.

the molten pool area, though there are some differences in the profiles away from the liquid pool, showing higher temperature for reduced emissivity, as expected. Figs. 9, 11 and 12 are consistent with the fact that most of the energy escapes from the pool by heat conduction through the part.

4. Summary of original results

The model developed in this work, although simple in its conception, has been able to capture several features of the thermal behavior of LENS-deposited parts, improving on prediction capability with respect to previous models. When properly calibrated to an experimental set up, the model confirms known experimental trends and delivers previously unknown thermal aspects of the process. In the following, we illustrate these points by referring to the figures in the text.

Fig. 4 shows that the temperature profile can be predicted reasonably well both within and outside the molten pool. The inclusion of the latent heat term in Eq. (5) is critical in order to capture the slope changes at the liquidus and solidus temperatures. In contrast with previous models, the temperature of the molten pool is not preset, but calculated. We must observe that we are still ignoring many of the complexities of the real process, like solid phase transformations, interface undercooling, kinetics effects, marangoni convection, mushy zone solidification, porosity, segregation, etc., which may affect the temperature profile.

Fig. 5 gives two important pieces of information. First, it provides a calculation of the amount of heat loss by convection and radiation along the entire top of the part, including the molten pool. Integration of these heat flux profiles allows a quantitative justification of the usual assumption of dominant heat conduction in the process. Second, it reveals a considerable radiation loss from the molten pool and surrounding area. Although this radiation may not be critical to the overall heat transfer in the part, it can certainly affect the phenomena occurring in the molten pool and the mushy zone, and it should be considered in any local pool model.

Fig. 6 provides a quantitative estimation of the edge effects, showing that the temperature profile is affected only within 5 mm from the edge. It also gives information of the temperature gradients away from the pool. Similar profiles were shown in Ref. [9] for a Ni-base alloy.

Figs. 7–12 contain the results of a new parametric study which convey significant insight in many aspects of LENS, some of which were discussed in the previous section. Particularly interesting are the effect of the latent heat (Fig. 10), neglected in previous models, and the change in temperature profiles with the heat transfer coefficients (Fig. 9). The latter represents a potentially useful guide for controlling the molten pool size by changing the gas flow from the powder nozzles. Also noteworthy is the result of Fig. 7, which clearly illustrates how the increase of laser power reduces the temperature gradient at the liquidus isotherm (1733 K) and consequently the cooling rate of the part.

Although the foregoing results with this simple model look encouraging, we must admit that there is still a long way to a model-controlled LENS. The actual process has many more variables that need to be considered, like selection of the deposition pattern, powder flow rates, nozzle angles, idle time between deposited layers, etc. To achieve the goal of controlling the residual stress in LENS-built parts, more comprehensive experimentally validated models are needed which incorporate microstructure prediction and microstructure-property relations in their constitutive equations.

5. Conclusions

A finite element thermal model was developed to calculate the temperature distribution in SS316 plates during fabrication by the LENS process. The model predicts temperature contours that agree qualitatively and quantitatively well with measured data. The effects of the plate vertical edges on the temperature contours were investigated. It was found that for the current process parameters, the temperature contour will reach a steady-state condition relative to a coordinate system attached to the moving laser beam when the laser beam moves to about 5 mm away from the part edges. A parametric study shows that the temperature profile in the melt pool is not significantly affected by small changes in thermal boundary conditions, the reason being that about 90% of the deposited laser energy is transported away from the pool by thermal conduction through the part. However, the laser power, thermal conductivity and its variation with temperature play an important role in the thermal profiles and the molten pool size.

Acknowledgements

The authors appreciate the sponsorship of the U.S. Army TACOM and the Center for Advanced Vehicular Systems (CAVS) of Mississippi State University.

References

[1] M.L. Griffith, M.E. Schlienger, L.D. Harwell, M.S. Oliver, M.D. Baldwin, M.T. Ensz, J.E. Smugeresky, M. Essien, J. Brooks, C.V. Robino, W.H. Hofmeister, M.J. Wert, D.V. Nelson, Proceedings of the Solid Freeform Fabrication Symposium, The University of Texas at Austin, Austin, TX, 1998, pp. 89–97.
[2] W. Hofmeister, M. Griffith, M. Ensz, J. Smugeresky, JOM 53 (2001) 30–34.
[3] M.L. Griffith, E. Schlienger, L.D. Harwell, M.S. Oliver, M.D. Baldwin, M.T. Ensz, J.E. Smugeresky, M. Essien, J. Brooks, C.V. Robino, W.H. Hofmeister, M.J. Wert, D.V. Nelson, J. Mater. Des. 20 (1999) 107–114.
[4] M.L. Griffith, M.T. Ensz, J.D. Puskar, C.V. Robino, J.A. Brooks, J.A. Philliber, J.E. Smugeresky, W.H. Hofmeister, Mater. Res. Soc. 625 (2000) 9–20.
[5] W. Hofmeister, M. Wert, J. Smugeresky, J.A. Philliber, M. Griffith, M.T. Ensz, JOM 51 (7) (1999).
[6] R. Ye, Y. Zhou, W. Wei, J.E. Smugeresky, E.J. Lavernia, TMS (2003) 369–376.
[7] L. Costa, R. Vilar, T. Reti, A.M. Deus, Acta Mater. 53 (2005) 3987–3999.
[8] M. Grujicic, G. Gao, R.S. Figliola, Appl. Surf. Sci. 183 (2001) 43–57.
[9] M. Grujicic, Y. Hu, G.M. Fadel, D.M. Keicher, J. Mater. Synth. Process 9 (2002) 223–233.
[10] D. Rosenthal, Trans. ASME 68 (1946) 849–866.
[11] A. Vasinonta, J.L. Beuth, M.L. Griffith, Proceedings of the Solid Freeform Fabrication Symposium, The University of Texas at Austin, Austin, TX, 2000.